High-Temperature Corrosion of Unpassivated Carbon Steel in Simulated Boiler Water: Electrochemical Thresholds and Mechanisms for Chloride and Sulphate Contamination

Benjamin A. Loder‡ and William G. Cook**

‡Corresponding author. E-mail: bloder@unb.ca.

*University of New Brunswick - Centre for Nuclear Energy Research (CNER), 2 Garland Court, Fredericton, New Brunswick, E3B 5A3, Canada

ABSTRACT

The presence of chloride (Cl^-) and sulphate (SO_4^{2-}) in boiler water poses a significant threat to carbon steel boiler tube integrity, yet their specific corrosion mechanisms and interaction at industrially relevant high temperatures remain poorly characterized. This study quantifies the accelerated corrosion thresholds and elucidates the distinct mechanistic roles of these contaminants for initially unpassivated SA210-A1 carbon steel exposed to simulated all-volatile treatment (AVT) boiler water at 310 °C and 10.3 MPa. In situ corrosion rates were measured using linear polarization resistance (LPR), supported by thermochemical equilibrium modelling (FactSage™). Results show that the corrosion threshold for SO_4^{2-} is approximately 1.5 to 3 times higher than for Cl^-, validating industry heuristics. Mechanistic analysis indicates that Cl^- is associated with lowering the solution pH which in turn increases iron solubility, while sulphate serves as an electron-accepting species under the high-temperature reducing conditions at 310 °C, where hydrothermal reduction to H_2S is thermodynamically favoured. Furthermore, the chemical form in which the contaminants were introduced strongly governs their combined behaviour. When introduced as ammonium salts, the combined threshold was higher than for individual Cl^- contamination, while mineral acid (HCl and H_2SO_4) additions resulted in a lower combined contamination threshold than that of Cl^- alone. Since ammonium salts do not reflect the acidic, deposit-controlled environments expected in operating boilers, mineral acid additions provide a more realistic representation of localized chemistry. These findings provide quantitative thresholds and mechanistic clarity that establish a foundational basis for improving water chemistry guidelines and models.

KEY WORDS: All-Volatile Treatment (AVT), Boiler Water Chemistry, Carbon Steel, Chloride-Induced Corrosion, High-Temperature Aqueous Corrosion, High Temperature Electrochemical Measurements, Linear Polarization Resistance (LPR), Sulphate Reduction, Thermochemistry Modelling

1 INTRODUCTION

Ionic species like chloride (Cl^-) and sulphate (SO_4^{2-}) are often found in boiler water as a result of leaks in condenser tubing or through the dissolution of ion exchange resins in the feedwater treatment plant [1], [2]. These species are considered contaminants due to their known effect of accelerating the corrosion of boiler materials, more specifically ferrous metals [2], and are of particular concern as they can acidify the boiler water in stagnant locations such as under deposits [3]. Most of the current literature [4], [5], [6], [7], [8], [9], [10], [11], [12] on the corrosion of boiler materials subjected to Cl^- and SO_4^{2-} contamination, describe work completed at temperatures below that of typical industrial operating conditions. While they provide some insight into the mechanisms of contaminant induced corrosion, it is common for boilers to operate above 300 °C, and few studies, particularly those using electrochemical techniques, have surpassed this temperature. In recognition of this, the

International Association for the Properties of Water and Steam (IAPWS) has emphasized that a better understanding of the corrosion mechanisms for such ionic contaminants in steam raising systems is still needed to support / improve cycle chemistry operating practices [13]. The Electric Power Research Institute (EPRI) identified this topic as a research priority and funded this research to address the knowledge gap.

Of the available literature, some interesting behaviour has been reported on the competition between Cl^- and SO_4^{2-} when both are present in solution. Niu et al [4], [5] has shown that the addition of SO_4^{2-} to a simulated all-volatile treatment (AVT) boiler water containing Cl^- can act to suppress pitting on 13Cr stainless steel at 90 °C. This was attributed to the formation of low solubility salt films that re-passivate sites from Cl^- pitting. Additionally, James et al. [14] in an investigation of corrosion fatigue crack initiation on SA210-A1 carbon steel subjected to contaminated boiler water at 275 °C, showed that the addition of SO_4^{2-} to Cl^- containing solution increased the number of required cyclic loads before cracking was induced. This limiting effect was shown to be consistent for both AVT and phosphate treatment boiler water chemistries. In each of the above studies, as is often the case, Cl^- and SO_4^{2-} were added to the solution as NaCl and Na_2SO_4.

This study aims to further investigate the mechanisms of Cl^- and SO_4^{2-} induced corrosion under conditions more representative of an operating boiler. To do so, the linear polarization resistance (LPR) method [15], [16], [17], [18], [19], [20] was employed to measure, in situ, the corrosion rates of unpassivated SA210-A1 boiler tube steel subjected to simulated AVT boiler water under various levels of Cl^- and SO_4^{2-} contamination. It is recognized that unpassivated steel does not exist in real operation; however, to elucidate the separate and combined effects of Cl^- and SO_4^{2-} anions, unpassivated steel was used as a starting point. Experiments were completed at 310 °C using AVT solutions contaminated with Cl^- or SO_4^{2-} individually, as well as a combination of both species. Additionally, trials were conducted with contaminant ions in the form of ammonium salts (NH_4Cl and $(NH_4)_2SO_4$), and later mineral acids (HCl and H_2SO_4), to better represent the chemistry conditions that may be present under deposits. To help better describe the influence of Cl^- and SO_4^{2-} on the observed corrosion behaviour and to compliment the experimental tests, simulations were completed using the FactSage™ thermochemistry modelling package [21]. This work is part of a longer-term initiative to provide accelerated corrosion thresholds for ionic contamination to better inform power cycle chemistry guidelines.

2 EXPERIMENTAL

2.1 Flow-through Electrochemical Cell

The electrochemical cell used in this study is of the three-electrode type, consisting of a platinum foil counter electrode (CE), SA210-A1 carbon steel working electrode (WE), and a platinum wire pseudo-reference electrode (RE). The CE is constructed from a ring of 0.5 mm thick platinum foil welded to a platinum wire (0.5 mm diameter), while the RE is a coiled piece of 0.5 mm diameter platinum wire. The WE-CE pair is contained within a 316 – stainless steel (SS) MHM4 Conax Technologies compression seal fitting. The WE-CE Conax assembly also contains a thermocouple to measure temperature at the fluid end of the probe. An exploded view of the WE-CE Conax assembly is shown in Figure 1, while Figure 2 shows the fluid end of the assembled WE-CE probe. The platinum wire portion of the CE that passes through the Conax fitting is insulated with PTFE heat shrink, while a small gap between the platinum foil and steel follower is maintained to prevent electrical contact at the fluid end. The carbon steel WE was isolated from the surrounding fitting using a yttria stabilized zirconia (YSZ) ceramic sheath in combination with PTFE heat shrink. Similar to the WE-CE assembly, the RE is contained within a separate 316-SS MHC2 Conax fitting and uses PTFE heat shrink to electrically isolate the platinum wire. The complete electrochemical cell is assembled by adding both the RE and WE-CE Conax components to a Swagelok 316-SS cross fitting, which serves as the body of the cell.

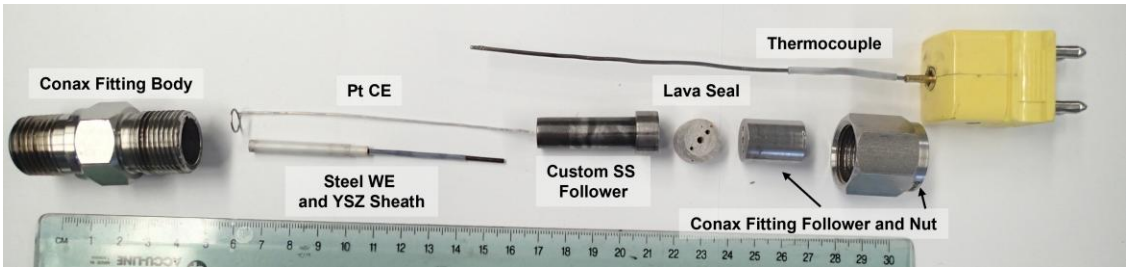

Figure 1. Exploded view of the WE-CE Conax assembly.

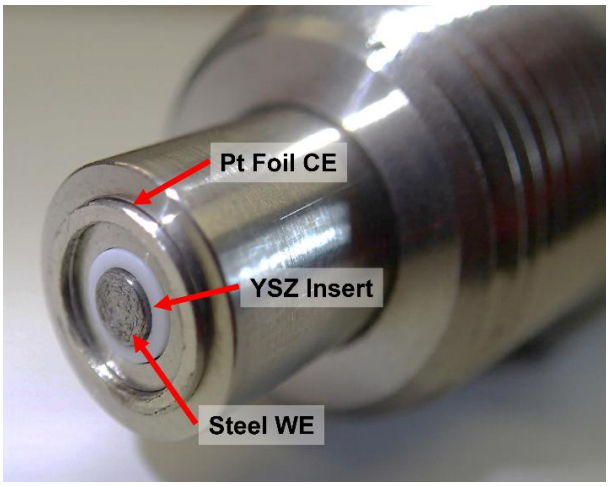

Figure 2. Close-up view of the WE-CE probe. Note that in this figure the carbon steel WE is not fully polished and there is no gap between the Pt foil / 316-SS follower as this is a mock-up assembly.

A once-through autoclave system (Figure 3) was used to facilitate testing within the electrochemical cell. Two 50 L Nalgene carboys provide separate storage of the uncontaminated and contaminated simulated AVT boiler water. Both carboys were continuously purged with argon gas to maintain a dissolved oxygen concentration below 10 µg/kg. Two parallel high performance liquid chromatography (HPLC) pumps (Eldex model 1HM) take fluid from each carboy. The flowrate of each pump was individually adjusted (0.01 mL/min resolution) depending on the desired contaminant concentration, to achieve a target total flow rate of 5.00 mL/min. The solutions from each HPLC pump are combined prior to entering a 300 mL Inconel 625 autoclave (Autoclave Engineers) to preheat the test solution to 310 °C upstream of the electrochemical cell. To offset heat losses between the autoclave and electrochemical cell, rope heaters were installed around the inlet tubing and cell body. After passing through the electrochemical cell, the solution temperature is lowered via a water-cooled shell and tube heat exchanger (test solution on the tube-side). The cooled solution then flows through a back-pressure regulator prior to discharging to the drain or to the sample collection line via a three-way valve. All wetted components (Swagelok tubing, valves and fittings) of the once-through test system apart from the carboys and autoclave, are constructed of 316L stainless steel.). All hot / pressurized components of the test apparatus are contained within a closed steel-framed cabinet as a safety measure, while also acting as a Faraday cage reducing EMF interference to the electrochemical cell. Concentrations of the ionic contaminant species were determined by collecting samples of the test rig effluent in 50 mL HPDE centrifuge tubes via the sample collection line, which were then analysed using a Dionex ICS-3000 Ion chromatography (IC) system.

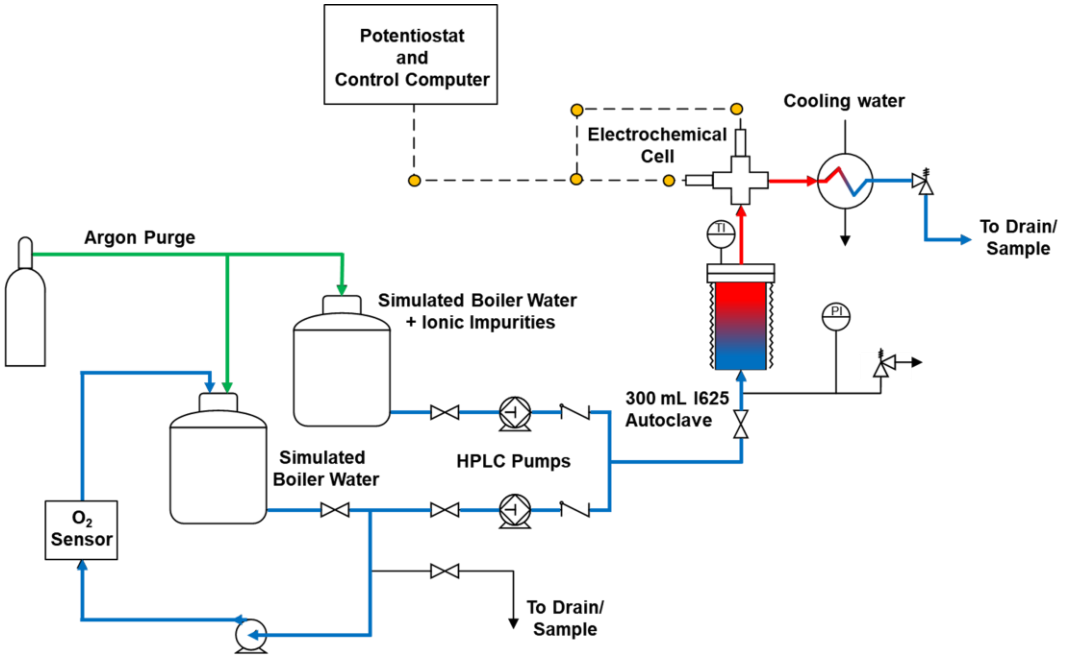

Figure 3. Simplified schematic diagram of the once-through autoclave test system.

2.2 *Steel Electrodes*

Boiler tube steel samples were prepared from SA210-A1 carbon steel with a composition (% w/w) of C 0.134%, Si 0.186%, Mn 0.683%, P 0.009%, S 0.004%, Cr 0.133%, Mo 0.038%, Ni 0.103%, Cu 0.143%, V 0.0025, balance Fe, machined into 90 mm long cylinders with two sections of different radii (1.5 mm and 0.88 mm). The steel stock used to machine the electrodes was provided in the form of a section of boiler tube from Siemens Heat Transfer Technology and all electrodes were manufactured by the Chemical Engineering department machine shop at the University of New Brunswick. The cross-sectional surface at the tip of the larger end of the cylinder was exposed to the test solution during experiments, while the non-exposed end connects to the electrical leads of the potentiostat. The edge at the transition between radii is seated against a matching edge within the custom YSZ insert / Conax follower to secure the electrode in place, preventing ejection from the fitting once pressurized. Before each experimental trial, the steel electrodes were mechanically polished to 1200 grit and rinsed with deionized water and ethanol to remove any oils or debris. Figure 4 shows an example of a freshly polished steel electrode.

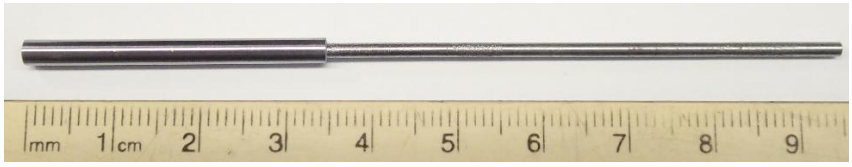

Figure 4. 1200 grit polished boiler tube steel (SA210-A1) working electrode.

2.3 *Preparation of Test Solutions*

Simulated boiler water was prepared by initially filling the two 50 L Nalgene reservoirs with 15 MΩ-cm deionized water. Each reservoir was then recirculated through mixed bed ion-exchange resin (Purolite UCW3700) for approximately 24 hours while sparging with argon gas to remove any trace impurities as well as any carbonate up-take while transferring the water.

Once purified, the pH was adjusted to 9.4 ± 0.05 at 25 °C by the injection of stock solutions of NH_4OH prepared by dilution from a standard solution of NH_4OH (28% w/w NH_3 basis, ACS reagent, Sigma-Aldrich). The Cl^- and SO_4^{2-} impurities were added to the contaminant reservoir as stock solutions of either NH_4Cl and $(NH_4)_2SO_4$ or HCl and H_2SO_4. The Ammonium chloride and ammonium sulphate stock solutions were prepared

gravimetrically from NH_4Cl (≥99.5%, ACS Reagent, Sigma-Aldrich) and $(NH_4)_2SO_4$ (≥99.0%, Sigma-Aldrich); while the mineral acid contaminant solutions were prepared by dilution from standard solutions of HCl (36.5% w/w, Certified ACS Plus, Fisher Chemical) and H_2SO_4 (95.0% w/w, Certified ACS Plus, Fisher Chemical). Grab samples of each test solution were taken to verify the pH and conductivity using a Fisherbrand Accumet XL500 benchtop pH / conductivity meter.

2.4 Electrochemical Measurements

The corrosion rate of the steel electrode was monitored through the collection of LPR measurements. Prior to a LPR measurement, the open circuit potential (OCP) was monitored for 60 seconds to check for stability within approximately ± 5 mV. This was done to ensure consistent results, since the electrochemical cell uses a platinum pseudo-reference electrode and drift in the measured electrochemical potential can complicate the collection of linear polarization data [22]. In addition to the OCP stability checks, a relatively wide overpotential range of approximately – 30 mV to + 10 mV was applied to the steel electrode during an LPR measurement to ensure that the scan crossed the zero-current potential, as this is a requirement for the determination of polarization resistance. However, as is typical for this technique, only data within ± 10 mV of the zero-current potential was used to determine the polarization resistance. All LPR scans were completed by progressing from cathodic to anodic overpotentials at a scan rate of 0.5 mV/second. The electrochemical measurements were performed using a Princeton Applied Research Versastat 3 potentiostat.

The measured polarization resistances were corrected for uncompensated resistance [23], [24], [25] to account for the increased solution conductivity with each stepwise increase in contaminant concentration. This was completed using calculated solution resistivities at 310 °C for each contaminant concentration and a known value of the cell constant through Equations (1) and (2)

$$R_P = R_m - R_u \quad (1)$$

$$R_u = \frac{\rho_{sol}}{K_{cell}} \quad (2)$$

where R_P is the corrected polarization resistance, R_m is the measured resistance from LPR, R_u is the uncompensated resistance, ρ_{sol} is the solution resistivity (in Ω-cm), and K_{cell} is the cell constant (in cm).

Solution resistivities for each contaminant concentration were estimated using the high-temperature speciation and ionic equilibria calculated with FactSage™, combined with high-temperature conductance data obtained from reference [26]. The electrochemical cell constant was determined in-situ by installing the cell in the once-through test system and pumping uncontaminated AVT solution at 5.00 mL/min and 25 °C. The solution resistance was obtained from electrochemical impedance spectroscopy (100 kHz to 0.1 Hz, 10 mV RMS perturbation) while the test solution conductivity (at 25 °C) was measured using a benchtop conductivity meter. The solution resistance, R_{sol}, and the solution conductivity, $\sigma_{25\,°C}$, were then used to calculate the cell constant according to Equation (3).

$$K_{cell} = \frac{R_{sol}}{\sigma} \quad (3)$$

Cathodic and anodic Tafel coefficients (β_c and β_a) of 231 mV/dec and 116 mV/dec respectively were used in the conversion of the LPR derived polarization resistance, R_P, to the corresponding corrosion current, i_{corr}, via the Stern-Geary equation [17], [18], [19], [20] shown by Equation (4).

$$i_{corr} = \frac{1}{2.303\, R_P \left[\frac{1}{\beta_a} + \frac{1}{|\beta_c|}\right]} \quad (4)$$

The Tafel coefficients were calculated using Equations (5) and (6) [27] at 310 °C for the hydrogen evolution and iron dissolution reactions respectively

$$\beta_c = \frac{2.303\ R\ T}{-\alpha\ n\ F} \quad (5)$$

$$\beta_a = \frac{2.303\ R\ T}{(1 - \alpha)\ n\ F} \quad (6)$$

where α is the symmetry coefficient of the specific charge transfer reaction (assumed to be 0.5), n is the number of electrons transferred per mol (n being 1 hydrogen evolution and 2 for iron dissolution), F is Faraday's constant (96,500 C mol^{-1}), R is the universal gas constant (8.314 J mol^{-1} K^{-1}), and T is the absolute temperature. From the corrosion current, the corrosion rate (penetration rate in µm/a) was evaluated through Faraday's law using Equation (7)

$$\text{Corrosion Rate} = \frac{i_{corr}\ t\ M}{n\ F\ \rho\ A} \quad (7)$$

where t is 31,536,000 seconds (1 calendar year), M and ρ are the molar mass and density of iron or 55.8 g/mol and 7.86 g/cm^3 (at 25 °C) respectively, n is equal to 2 (iron dissolution), and A is the electrode area at the interface.

The corrosion rates were calculated assuming that the entire geometric surface area (3.275 cm2) of the larger diameter end of the electrode (see Figure 4) is exposed to the test solution (not including the cross-sectional area at the non-fluid end). Although the original design intended to isolate only the cross-sectional tip of the electrode, sub-millimetre gaps between the YSZ sheath and the electrode prevented reliable masking, therefore the full surface area was used for the calculations to ensure a consistent basis. Where the true active area exposed to the test solution is less than the full geometric surface area, which may occur in trials where the gaps between the YSZ sheath and electrode result in partial rather than full lateral exposure, the corrosion rates will be underestimated relative to the true value. The reported absolute rates should therefore be interpreted as lower bound estimates.

Despite this uncertainty in the absolute corrosion rate magnitudes, assuming a fixed geometric surface area does not affect the identification of the accelerated corrosion threshold. Although the net corrosion rate is proportional to the active surface area, the active area would only increase significantly, for example through surface roughening, if the electrode were already undergoing active corrosion. At the start of each experiment, the carbon steel electrode has a 1200 grit surface finish, upon exposure to the high temperature deaerated AVT water, rapidly develops a protective magnetite film. Under these initial conditions any measured Cl^- or SO_4^{2-} represents only trace contamination in the test solution. While oxide growth increases the true surface roughness and thus the total surface area, the oxide covered regions are passive and do not contribute to the active electrochemical area. Thus, the active area and therefore the net corrosion current, remains effectively constant until active corrosion begins. Any significant increase in active area would occur only after the accelerated corrosion threshold has been exceeded. Consequently, an apparent spike in the corrosion rate due to an increasing active area can not occur before the threshold; it can only influence the magnitude of the corrosion rate after the transition. Therefore, while assuming a fixed geometric surface area may potentially overestimate the absolute corrosion rate once active corrosion is underway (given that surface has roughened as a result), it does not create a false threshold or shift the threshold concentration, and the interpretation of the corrosion rate trends remains unaffected.

2.5 Accelerated Corrosion Threshold Testing

During each trial, the contaminant concentration in the test solution supplied to the electrochemical was increased stepwise until the maximum concentration contained in the contaminated simulated boiler water carboy was reached. For each incremental step, the electrochemical cell was allowed to stabilize for approximately 12 hours prior to the collection of electrochemical data and collection of grab samples from the test rig effluent. All tests were conducted at 310 °C and 10.3 MPa.

Each data point in the corrosion rate trends represents the average of at least two (typically three to four) consecutive LPR measurements collected at the same contaminant concentration. Between each measurement, the stability of the cell was verified by an OCP check as described previously. The error bars shown, represent the within-run measurement variability of these repeated LPR scans and are not intended to indicate statistical uncertainty or between-run reproducibility.

For each trial, the accelerated corrosion threshold was identified as the point at which either of the following two criteria were met: (i) in cases where the corrosion rate was observed to gradually decrease over the initial concentration step changes, the accelerated corrosion threshold was interpreted as the point at which a sustained change in the overall direction of the corrosion rate trend occurred, i.e., decreasing trend transitioning to a continually increasing trend, or; (ii) when the corrosion rate remained relatively stable over the initial concentration step changes, the accelerated corrosion threshold was taken as the concentration where a net increase of ≥ 5 % occurred, provided that the corrosion rate continued to climb as contaminant concentrations were further increased.

3 RESULTS AND DISCUSSION

Both individual and combined contaminant trials were completed under AVT chemistry on initially unpassivated steel electrodes, with this series of trials first carried out using ammonium salts, then repeated by adding the contaminants as mineral acids. Originally, the intent was to complete only the trials using the ammonium salt form of the contaminants to match the composition of the uncontaminated AVT test solution. Since NH_4^+ is already present in AVT solution, this form of contamination would not introduce additional cations like Na^+. However, after completing the initial series of experiments this approach was revaluated given that, in an actual boiler, ionic contaminants accumulate under deposits resulting in relatively acidic localized chemistry [3]. Since the present experimental methodology did not include initial passive oxides or deposits on the steel samples, the addition of Cl^- and SO_4^{2-} contaminants in mineral acid form was thought to better represent these conditions. In this approach, the pH of the test solution corresponds more directly to the contaminant concentration, therefore it is a closer representation of the system beneath a deposit layer without the need for the actual deposit.

Representative LPR scans collected during the individual NH_4Cl contamination trial are shown in Figure 5 to illustrate the behaviour of the steel electrode as the Cl^- concentration approached, reached, and exceeded the accelerated corrosion threshold. Prior to the accelerated corrosion threshold (Figure 5a), a clear and linear region exists within approximately ± 10 mV of the zero-current potential, indicating that the applied -30 mV to + 10 mV overpotential window does not significantly disturb the passivating surface. At the threshold concentration (Figure 5b), the slope (Δ I / Δ E) near the zero-current potential increases slightly, consistent with a reduction in polarization resistance (ΔE / ΔI) as the steel transitions away from passivity. Once the threshold is exceeded (Figure 5c), the measured currents increase and notable divergences appear between repeated scans, reflecting reduced surface stability and the transition toward active corrosion. In addition to the changing polarization resistance, the respective scans in Figure 5 demonstrate the shift of the steel electrode corrosion potential to more anodic values as the concentration of Cl^- increased, which is consistent with expectations for the onset of active corrosion. Overall, these scans indicate that the selected overpotential

range and stability of the electrochemical cell is suitable for capturing changes in the polarization resistance associated with the passive to active transition.

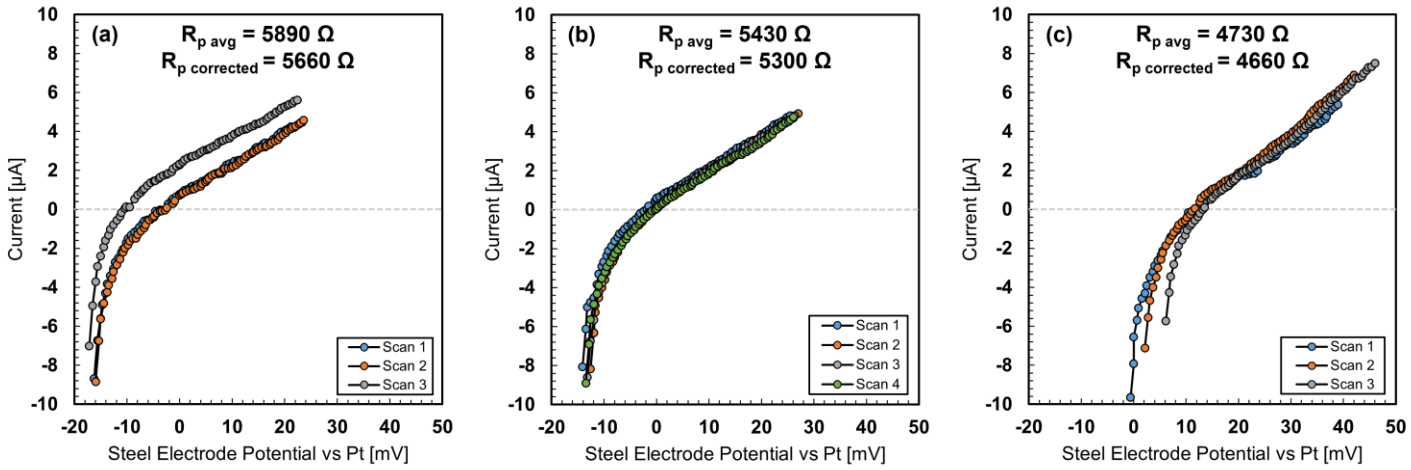

Figure 5. Example LPR scans taken during the individual NH_4Cl contaminant trial, where (a) is immediately before the corrosion threshold (150 µg/kg Cl^-), (b) is at the suspected threshold (390 µg/kg Cl^-), and (C) is past the threshold (770 µg/kg Cl^-).

The LPR scans shown in Figure 5 are representative of the electrochemical behaviour observed across all trials, with the passive to active transition captured consistently for each contaminant tested, and this transition point being defined as the accelerated corrosion threshold. The resulting corrosion rate trends are shown in Figure 6 and Figure 7 for tests completed with ammonium salts and mineral acids respectively. A summary of the accelerated corrosion thresholds observed for each trial are listed in Table 1.

When analysing the LPR data, the overall magnitude of the corrosion rates varied between each trial, with the biggest deviation being the trials completed with H_2SO_4 and combined HCl and H_2SO_4. These differences should not be attributed to the type of contaminant ion or source of contamination species (NH_4^+ salts vs mineral acids), since at the start of each test the electrodes are exposed to uncontaminated AVT solution. Given that the initial solution chemistry is virtually identical between trials except for trace contamination, and the steel electrodes are all polished within a reasonable degree of consistency up to 1200 grit, it would be expected that the corrosion rates in the uncontaminated AVT solution would also be similar. While a range of corrosion rates over approximately 10 to 30 µm/a across all trials apart from the aforementioned seems relatively reasonable, the increase to upwards of 120 µm/a seen for the H_2SO_4 and combined HCl and H_2SO_4 is excessive. This deviation is a further indication of the inconsistencies in the steel electrode surface area exposed to the test solution arising from the gaps between the electrode and YSZ sheath described previously. Given that the entire geometric surface area was used in the corrosion rate calculations, the uncontaminated corrosion rates observed for the H_2SO_4 and combined HCl and H_2SO_4 tests may represent the conservative case where the entire surface area is indeed active. From this, it is likely that the active area in the other trials is less than the assumed 3.275 cm^2, which artificially suppresses the calculated corrosion rate. While this makes the exact values of the corrosion rates difficult to interpret between trials, the net change and therefore the identification of the accelerated corrosion thresholds are not affected.

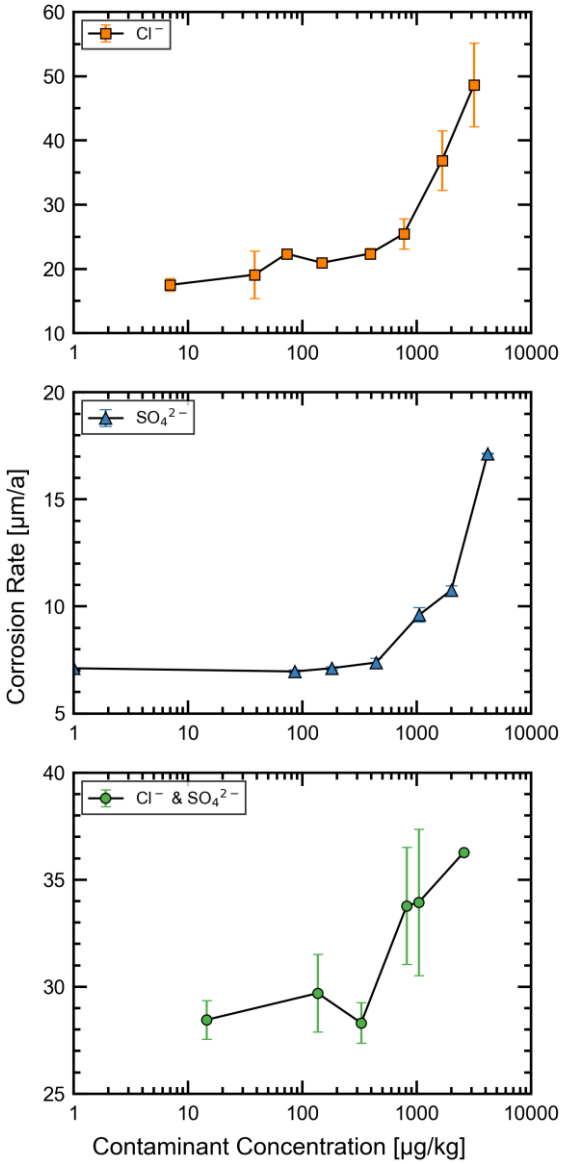

Figure 6. Corrosion rate trends from LPR measurements taken on initially unpassivated steel exposed to ammonium salt contaminants. Note that for the combined Cl^- & SO_4^{2-} trial $[Cl^-]$ is shown, while $[SO_4^{2-}] = 1.7 \times [Cl^-]$. Zero contamination is shown as 1 µg/kg due to the log scale.

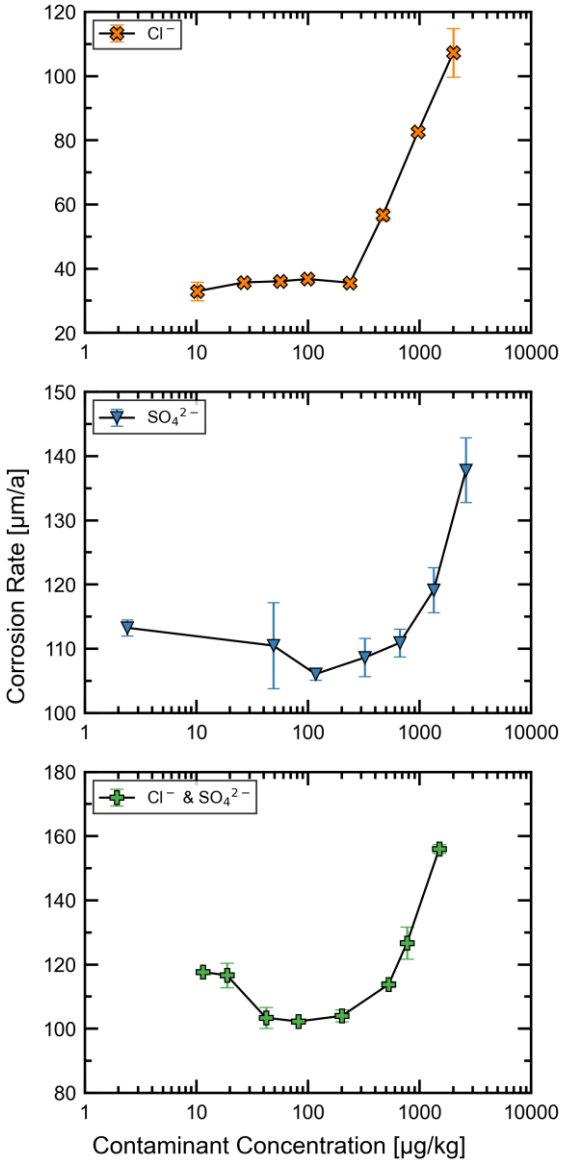

Figure 7. Corrosion rate trends from LPR measurements taken on initially unpassivated steel exposed to acidic contaminants. Note that for the combined Cl^- & SO_4^{2-} trial $[Cl^-]$ is shown, while $[SO_4^{2-}] = 1.5 \times [Cl^-]$. Zero contamination is shown as 1 µg/kg due to the log scale.

Comparing the corrosion rate trends measured for the individual contaminants, the accelerated corrosion threshold for SO_4^{2-} is approximately 1.5 – 3 times higher than for Cl^-, with the ammonia salt and mineral acid contaminants representing the lower and upper ends of this range respectively. The typical assumption used within the thermal power generation industry is that Cl^- is approximately twice as corrosive as SO_4^{2-}, therefore, concentration limits for SO_4^{2-} are often listed as simply 2 times the maximum allowable Cl^- specification [28]. This heuristic appears to be relatively consistent with the experimental results shown here. The accelerated corrosion thresholds for individual Cl^- contamination also show reasonable agreement to a value of approximately 200 µg/kg reported by Xiong et al. [9], derived from weight loss measurements on carbon steel exposed to static autoclave testing at 300 °C. The results from the combined contaminant trials showed that when the contaminants are added as ammonium salts, the accelerated corrosion threshold for the combined Cl^- and SO_4^{2-} is closer to the threshold for individual SO_4^{2-} contamination. In contrast to this, when added as mineral acids, the accelerated corrosion threshold aligns closer to that for individual Cl^-.

Table 1. Summary of the LPR derived accelerated corrosion threshold contaminant concentrations in AVT solution at 310 °C.

Contaminant Type	Species	LPR Corrosion Threshold in (µg/kg): Cl^- / SO_4^{2-}
Ammonium Salts	Cl^-	150 – 770 (potentially as low as 390[1])
	SO_4^{2-}	440 – 1050
	Cl^- & SO_4^{2-}	330 – 820 / 560 – 1400
Mineral Acids	Cl^-	240 – 470
	SO_4^{2-}	320 – 1340 (potentially as low as 670[2])
	Cl^- & SO_4^{2-}	200 – 530 / 300 – 870

To help investigate these differences, the FactSage™ Equilib thermochemistry modelling package [21] was used to simulate the iron-water system when exposed to the various types of Cl^- and SO_4^{2-} contamination under the conditions used within the experimental trials. For each contaminant type, the injected Cl^-, and SO_4^{2-} (NH_4^+ salt or mineral acid form) concentrations from each corrosion threshold trial at 310 °C were used as model inputs, along with an ammonia concentration of 1 mg/kg (corresponding to an uncontaminated $pH_{25\,°C}$ of ~ 9.4) and a dissolved O_2 concentration of 10 µg/kg. For combined Cl^- and SO_4^{2-} contamination, simulations were completed at several $[SO_4^{2-}]$ to $[Cl^-]$ ratios, to elucidate any interactions between the two contaminant ions. In all simulations, an excess of solid iron (0.5 mol) was assumed to be in contact with the solution (1 kg basis) to mimic the presence of the initially unpassivated carbon steel electrode. This value was chosen to maintain an excess of iron, so that the calculated concentrations of dissolved iron species in the solution represent their solubility limit corresponding to the given solution chemistry. Within the FactSage Equilib module, the Fact pure substances (FactPS), FACT oxide spinel compound (FToxid-SPINA), and the FACT aqueous (FThelg-AQID) ideal dilute solution (valid up to 0.001 molal, 350 °C and 165 bar) databases were selected to accurately represent the high temperature hydrothermal chemistry within the test system / electrochemical cell. An example of the FactSage™ Equilib model input, is shown for the combined contamination (NH_4^+ salt) trial at a $[SO_4^{2-}]$ / $[Cl^-]$ ratio of 1.7 in Table 2, while Figure 8 shows the resulting high temperature speciation against the injected contaminant concentration (as measured at 25 °C). Note that the lower molal concentration limits in Figure 8 have been cropped to 10^{-10} mol/kg. While some species are still predicted below this value, at such a low molality they can not be reasonably assumed to have an appreciable impact on the solution chemistry and corrosion behaviour of the steel. Also note that gaseous phase species are plotted as their partial pressures in units of atmospheres, where the total system pressure is 102 atm (10.3 MPa). Using this modeling approach, the pH_T values and total iron solubilities at 310 °C were calculated for each trial, the results of which are shown in Figure 9a and Figure 9c for the ammonium salt tests while the mineral acid tests are shown in Figure 9b and Figure 9d.

[1] Overlapping error bars between corrosion rate data points at 150 µg/kg and 390 µg/kg Cl^- make this uncertain.

[2] Overlapping error bars between corrosion rate data points at 320 µg/kg and 670 µg/kg SO_4^{2-} make this uncertain.

Table 2. FactSage Equilib model input parameters for the combined NH_4^+ contaminants at a SO_4^{2-} / Cl^- ratio of 1.7.

Temperature	Pressure	Initial Species Molality (mol/kg) at 25 °C and 1 atm					
(K)	(atm)	H_2O	Fe	NH_4Cl	$(NH_4)_2SO_4$	NH_3	O_2
583	102	55.5	0.50	0	0	6.28E-05	3.13E-07
				7.05E-07	4.42E-07		
				1.41E-06	8.85E-07		
				2.82E-06	1.77E-06		
				5.64E-06	3.54E-06		
				1.41E-05	8.85E-06		
				2.82E-05	1.77E-05		
				5.64E-05	3.54E-05		

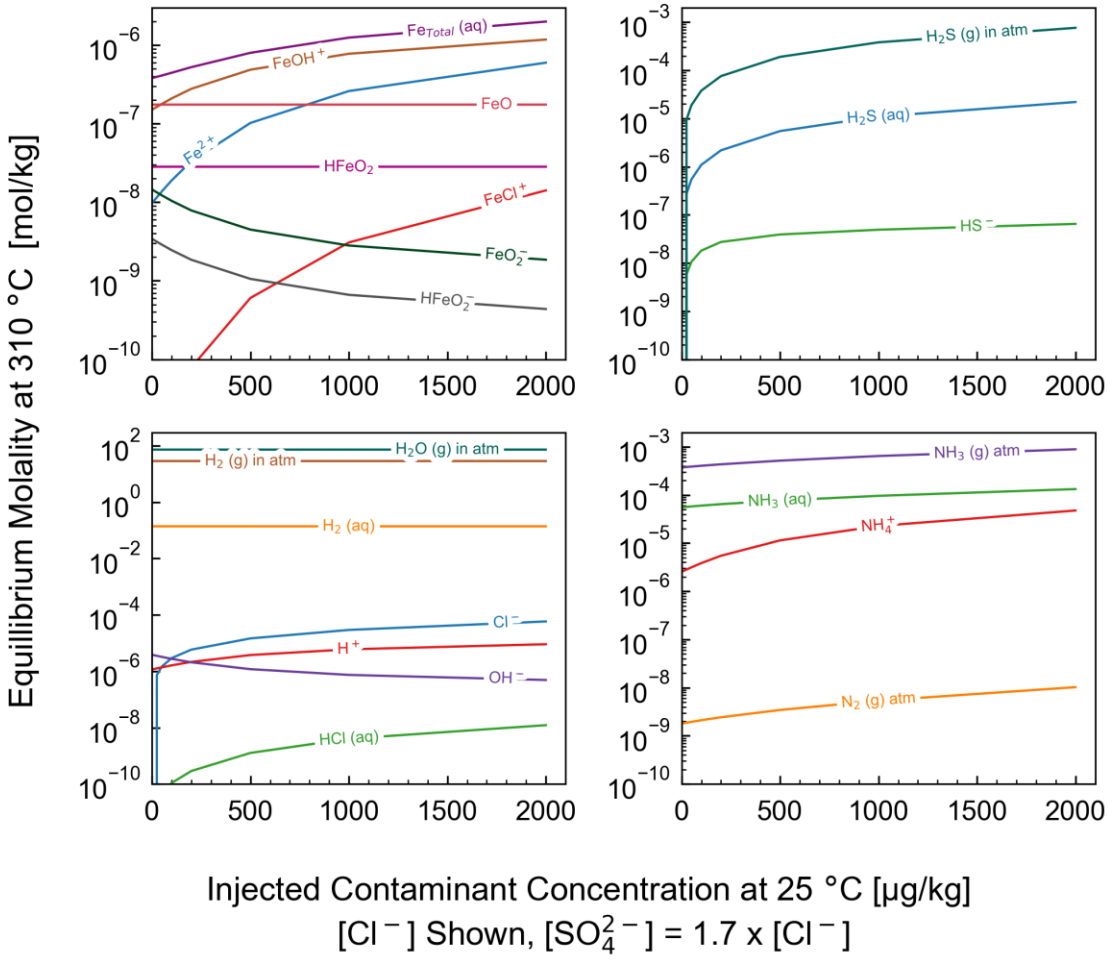

Figure 8. Equilibrium concentrations of relevant species simulated in FactSage™ for the combined NH_4^+ contaminant trial at a $[SO_4^{2-}]$ / $[Cl^-]$ ratio of 1.7x at 310 °C and 10.3 MPa (102 atm). Note that the gaseous species as denoted by (g) are plotted in units of atm. The solubility of total iron, indicated as Fe_{Total} (aq) in the first subplot, is taken as the sum of all dissolved iron species.

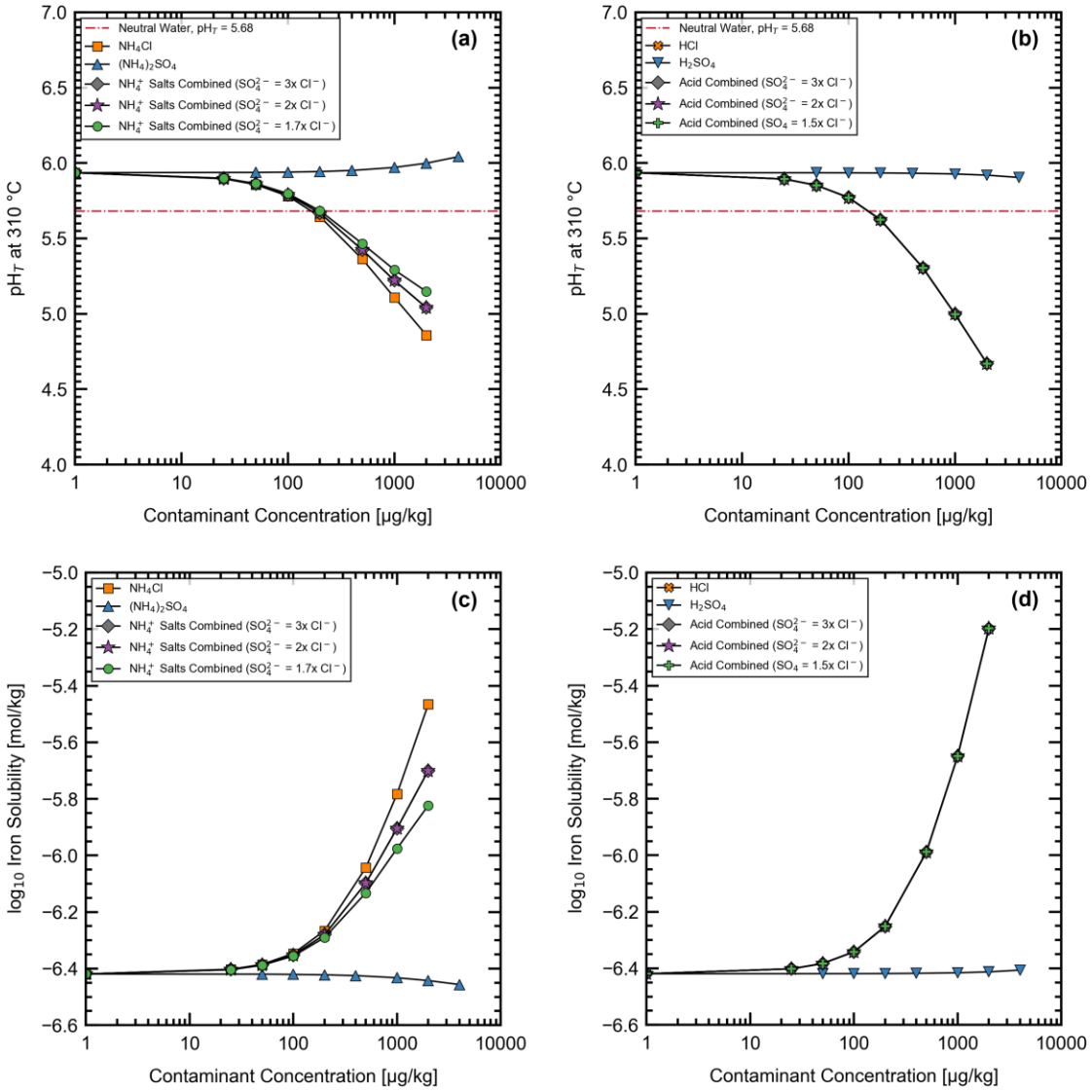

Figure 9. Calculated pH_T for the (a) ammonium salt and (b) mineral acid contaminants, along with the calculated total iron solubilities at 310 °C for (c) ammonium salt and (d) mineral acid contaminants. Note that for combined contaminants the solubilities are plotted against the Cl^- concentration. Zero contamination is shown as 1 µg/kg due to the log scale.

3.1 Chloride Corrosion Behaviour

The rates of iron / magnetite dissolution and precipitation are governed by their solubility [29], [30], where the concentration gradient between the surface of the steel / oxide film and the bulk solution is a major driving force behind the rate of both processes. Therefore, with increased solubility, it can be expected that the rate of iron dissolution will follow. As shown from the equilibrium modeling results in Figure 9 the Cl^- contamination very clearly increases the solubility of iron. This holds true whether it is first introduced as NH_4Cl or HCl. The underlying cause of this increase is suspected to be a result of several factors. First, at elevated temperatures, either of the two Cl^- containing species will acidify the solution as shown by the calculated pH_T trends in Figure 9. Since the pH of uncontaminated AVT boiler water is only slightly alkaline at 310 °C, decreasing the pH will increase the solubility of iron / magnetite as experimentally demonstrated in various other studies [31], [32], [33].

Second, it is well known that Cl^- solutions will form highly soluble complexes with iron. The formation of which prevents the complexed iron from reprecipitating as magnetite at the surface of the steel by carrying it away in the bulk solution [34]. When Cl^- is present at a high enough concentration, this complex formation is likely to have an effect on the total amount of dissolved iron. This was supported by the FactSage™

simulations, which showed that the formation of $FeCl^+$ became increasingly favourable beyond a Cl^- concentration of 200 to 500 µg/kg, approximately the experimentally measured accelerated corrosion thresholds for both forms of contamination. This is shown for the ammonium salt and mineral acid trials in Figure 10a and Figure 10b respectively. However, compared to the impact of pH_T, the increase in dissolved iron due to the formation of $FeCl^+$ only constitutes a fraction of the overall iron solubility.

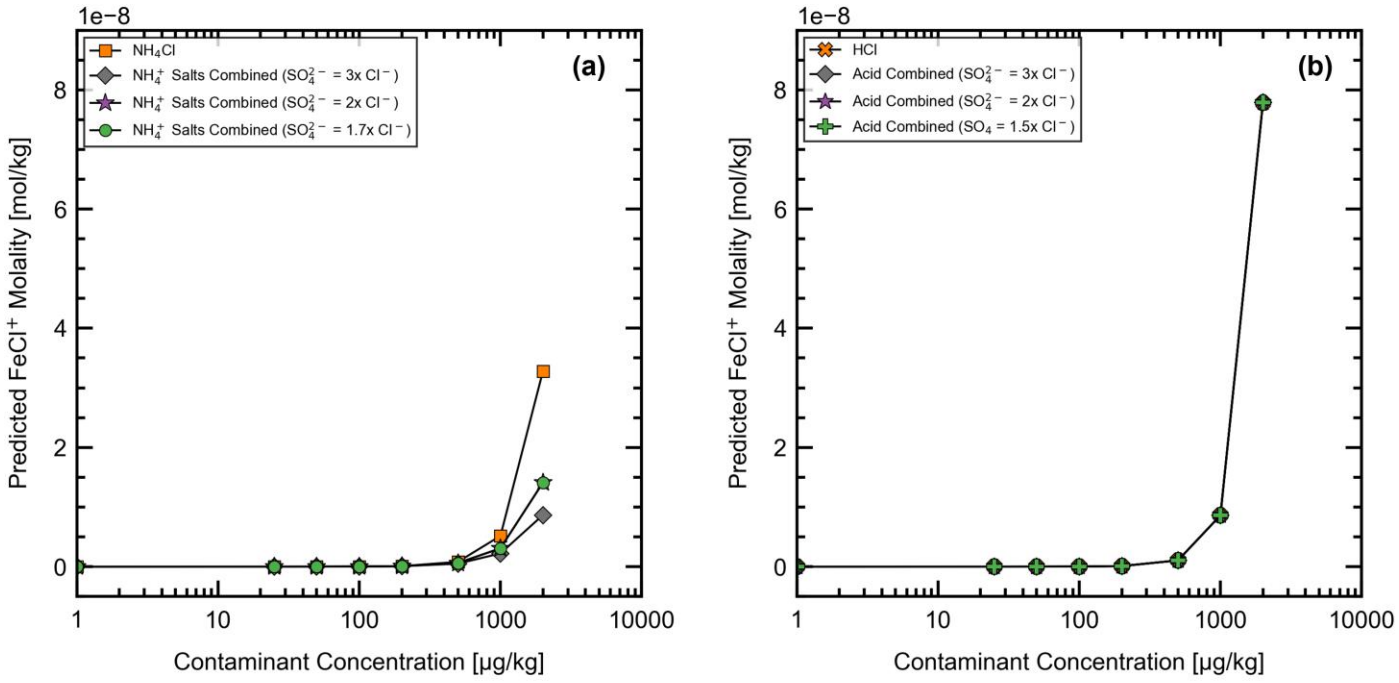

Figure 10. Predicted $FeCl^+$ molality at 310 °C for (a) ammonium salt and (b) acidic contaminants. Note that for combined contaminants the solubilities are plotted against the Cl^- concentration. Zero contamination is shown as 1 µg/kg due to the log scale.

Additionally, the outermost surface of an oxide film in contact with an aqueous solution is covered with a layer of hydroxyl groups. In acidic solutions, these hydroxyl groups interact with protons to form a positive surface charge [22], [35], [36]. The adsorption of Cl^- due to coulombic attraction will act to depolarize the surface allowing protons to more readily participate in hydrogen reduction as they are no longer repelled by the positive charge [22], [35], [37]. As a result, iron dissolution is accelerated. While the steel electrode lacks a protective oxide film at the beginning of each trial, upon exposure to the high temperature solution the surface will quickly begin to passivate. Each of the factors discussed above will affect the rate at which this passivation process can proceed. Therefore, the accelerated corrosion threshold can then be said to represent the point at which the rate of the Cl^- assisted iron / magnetite dissolution dominates over the rate of passivation. Additionally, as demonstrated by Zhang et al. [38], the incorporation of Cl^- into the barrier layer of magnetite as it grows on the steel's surface, can potentially negate the protection it would normally provide.

3.2 Sulphate Corrosion Behaviour

It is clear from Figure 9 that whether added in ammonium salt or mineral acid form, SO_4^{2-} has a negligible effect on the pH_T and by extension the solubility of iron, at least within the tested concentration range. In fact, when added as $(NH_4)_2SO_4$ the calculated iron solubility decreases slightly as the SO_4^{2-} concentration is increased, with this being a result of the pH_T shifting slightly more alkaline. This indicates that in contrast to the behaviour observed for Cl^- contamination, the influence of SO_4^{2-} on carbon steel corrosion must arise primarily from kinetic effects rather than from an increased thermodynamic driving force for dissolution.

However, the absence of a solubility increase does not imply that the dissolution rate must remain constant in SO_4^{2-} containing solutions, as evidenced by the corrosion rate trends in Figure 6 and Figure 7. Under flowing conditions, where the solution at the electrode is continuously refreshed, the dissolved iron concentration in the bulk solution is unlikely to approach its solubility. Therefore, the corrosion rate is not strictly solubility limited and instead is governed by the balance between anodic iron dissolution and the available cathodic reactions. In Cl^- containing solutions, hydrogen reduction is the only available cathodic reaction, so the increased iron solubility provided by the impact of the Cl^- on the pH, accelerates dissolution when the solubility limit is not yet reached in the bulk. In SO_4^{2-} containing solutions, although the solubility does not increase, SO_4^{2-} introduces an additional cathodic reaction pathway through its reduction to H_2S. This increases the total cathodic current, which requires a corresponding increase in the iron dissolution rate and thus, the corrosion rate.

The FactSage™ simulations represent equilibrium conditions where an excess of iron is assumed to be present to force the solution to its solubility limit. These values therefore represent an upper bound on dissolved iron concentration. In the experiments, the system is unlikely to approach this solubility limit, so the corrosion rate is controlled by electrochemical kinetics rather than solely by solubility constraints. For these reasons, the observed increase in dissolution rate with SO_4^{2-} is fully consistent with the mechanistic framework, even though the predicted solubility remains constant.

Under hydrothermal conditions it has been demonstrated that SO_4^{2-} is reduced to H_2S by coupling with the oxidation of dissolved H_2 as described by Equation (8) [39].

$$4\ H_{2\,(g)} + SO_{4\,(aq)}^{2-} + 2\ H_{(aq)}^{+} \rightleftharpoons H_2S_{(g)} + 4\ H_2O_{(l)} \quad (8)$$

The simulations completed in FactSage™ also showed that sulphate reduction is predicted whether it is added as $(NH_4)_2SO_4$ or H_2SO_4. At high temperatures, sulphate exists predominantly as the bisulphate (HSO_4^-) anion [40], however, with the presence of an excess of iron, the sulphate containing species were predicted to undergo virtually complete reduction to H_2S and exist in equilibrium between aqueous H_2S and the bisulphide anion (HS^-) as shown in the example high temperature speciation trends in Figure 8. From this, it is hypothesized that the in the presence of carbon steel, reduction of the HSO_4^- could at least partially couple with the dissolution of iron as a source of electrons through the following half-cell reaction:

$$HSO_{4\,(aq)}^{-} + 9\ H_{(aq)}^{+} + 8\ e^- \rightleftharpoons H_2S_{(aq)} + 4\ H_2O_{(l)} \quad (9)$$

The electrode potential of the half-cell reaction in Equation (9), was calculated using the Nernst equation. At 310 °C, the resulting potential ranged from -33 mV to -37 mV (vs SHE), depending on whether the standard potential, E^o (310 °C), was directly obtained from FactSage™ at the test conditions (the former), or calculated from published standard Gibbs energies of formation, followed by a temperature correction to 310 °C via the Gibbs-Helmholtz relation (the later). To represent conditions where only SO_4^{2-} was added, a pH 310 °C of 5.9 was used in the Nernst calculation. For simplicity, the activities of H_2S and HSO_4^- were assumed to be equal. Under the same conditions, i.e., pH 310 °C of 5.9 and a hydrogen partial pressure of 28.7 atm (predicted by FactSage™, see Figure 8), the electrode potential for hydrogen reduction was calculated at -77 mV (vs SHE). Given that the electrode potential of the bisulphate reduction is more positive than that of hydrogen evolution under these conditions, it is plausible that this half-cell reaction could couple with iron dissolution. However, since SO_4^{2-} / HSO_4^- reduction can occur even without the presence of iron [39], it is likely that the reaction represented by Equation (8) is the dominant pathway, and it is only at relatively high injected concentrations of SO_4^{2-} that the amount reduced through Equation (9) has any appreciable impact on iron dissolution. From this, it would be expected that the accelerated corrosion threshold for individual SO_4^{2-} contamination should be higher than for Cl^-, with this being supported by the results of the experimental trials. The increasing pH_T shown for additions of $(NH_4)_2SO_4$ in Figure 9a can also be explained by the consumption of H^+

when SO_4^{2-} / HSO_4^{2-} is reduced to H_2S. Unlike H_2SO_4, which directly adds H^+ to the system, the dissociation of $(NH_4)_2SO_4$ contributes to an equilibrium between NH_4^+ and NH_3. Although this equilibrium is highly shifted towards NH_3 at elevated temperatures [3], [42], [43], [44], [45], fewer protons are released than for H_2SO_4, and the overall effect of the SO_4^{2-} reduction results in a slight loss of H^+.

3.3 Combined Chloride and Sulphate Corrosion Behaviour

When Cl^- and SO_4^{2-} are combined, the impact of contamination on the corrosion of the carbon steel is more complex. This is particularly evident, as the form in which the contaminant species are introduced appears to influence their overall behaviour. When added as HCl and H_2SO_4 there is no distinct difference in the pH_T and therefore the iron solubility (Figure 9b and Figure 9d) between a combination of Cl^- and SO_4^{2-} or Cl^- alone. This was found to be consistent even when the ratio between the two species was adjusted in the FactSage™ simulations.

In contrast to this, when compared to individual NH_4Cl contamination, the addition of $(NH_4)_2SO_4$ reduces the overall impact of the mixture on the pH_T and therefore the iron solubility (Figure 9a and Figure 9c). Interestingly, the simulations showed that increasing the ratio of SO_4^{2-} to Cl^- further dampens any change. As shown previously in Table 1, the accelerated corrosion threshold of the combined contaminants was higher than for either individual species. This suggests that when added as ammonium salts, SO_4^{2-} will suppress the corrosive behaviour of Cl^-.

Despite numerous studies [4], [5], [14], [34], [46], [47], [48], [49], [50], [51] reporting similar limiting effects of the SO_4^{2-} ion on the corrosion of steels in Cl^- solutions, the exact cause has remained speculative. Unfortunately, no post exposure surface analysis of the steel electrodes was completed in this present study. Therefore, it is unknown whether the formation of protective iron SO_4^{2-} salt films like those reported elsewhere [4], [5], [46], [49], [51] had occurred. In addition, the concentration of contaminants in these studies were reported to be on the order of 100 mg/kg up to several parts per thousand (g/kg), which is far higher than typical for boiler water even under contaminant excursion conditions. It is also unknown if the precipitation of these species would be favourable at 310 °C, as most other works have been completed below 100 °C. Notably, no such species were predicted by the simulations performed in FactSage™.

Based on the analysis of the individual contaminant trials, it is more likely that the reduction of SO_4^{2-} when added as $(NH_4)_2SO_4$ slightly buffers the acidity of the Cl^-. Since the effect of Cl^- contamination on the corrosion behaviour of initially unpassivated steel appears to be primarily a factor of increasing the solubility of iron through lowering the pH, the addition of $(NH_4)_2SO_4$ acts to delay the accelerated corrosion threshold. When added as HCl and H_2SO_4, although the reduction of SO_4^{2-} reduces the effective acidity of the H_2SO_4, there is still a net gain of protons. Therefore, the accelerated corrosion threshold of the combined contaminants is slightly lower than that for the individual HCl contamination.

3.4 Practical Considerations

As previously noted, in real operation, unpassivated or bare steel boiler tube surfaces do not occur. Accordingly, the accelerated corrosion threshold concentrations presented in Table 1 are most valuable for (i) advancing the understanding of Cl^- and SO_4^{2-} corrosion behaviour at high temperature, and (ii) demonstrating the capabilities of the high-temperature electrochemical cell. They should not, however, be interpreted as shutdown limits for boiler water. This distinction arises due to two factors:

(i) Real boiler tube surfaces are protected by a magnetite layer; thus, the contaminant concentrations required to induce accelerated corrosion (i.e., passive film breakdown) are expected to be significantly higher than the values reported in Table 1.

(ii) Boiler water shutdown limits are based on ionic contamination in the boiler drum blowdown stream. Due to their low volatility and solubility in the steam phase, species like Cl^- and SO_4^{2-} concentrate beneath boiler tube deposits subjected to a high heat flux, producing local environments with orders of magnitude higher contaminant concentrations than those measured in the bulk boiler water. Evaluating shutdown limits therefore requires accounting for this concentrating effect at the passivated boiler tube surface.

It was also observed that when added as ammonium salts, SO_4^{2-} buffered the acidification of the test solution from Cl^-, producing a higher accelerated corrosion threshold concentration for combined NH_4Cl and $(NH_4)_2SO_4$ relative to NH_4Cl alone. It is unlikely, however, that NH_4Cl or $(NH_4)_2SO_4$ would form or be present in a boiler. Although ammonium salts were originally selected to avoid introducing additional cations into the AVT test solutions, these results indicate that their use can create unique high-temperature chemistry not representative of boiler operation. For future studies, mineral acids should be preferred as contaminant sources over both ammonium and sodium salts, as they more accurately simulate the localized chemistry beneath boiler tube deposits. This consideration is particularly important if synthetic deposits and high heat flux exposure cannot be combined with electrochemical measurement techniques.

4 CONCLUSIONS

- The accelerated corrosion thresholds for chloride and sulphate were successfully quantified for initially unpassivated SA210-A1 carbon steel at 310 °C and 10.3 MPa. It was found that the accelerated corrosion threshold for individual SO_4^{2-} contamination is approximately 1.5 – 3 times higher (depending on the initial form of the contamination) than for Cl^-, supporting the long standing industry heuristic that Cl^- is approximately twice as corrosive as SO_4^{2-}.

- Chloride accelerates corrosion primarily through thermodynamic effects. FactSage™ modeling and electrochemical corrosion rate measurements show that Cl^- lowers solution pH which in turn increases iron solubility, thereby increasing the thermodynamic driving force for dissolution and shifting the steel towards active corrosion.

- Sulphate accelerates corrosion through kinetic, rather than thermodynamic mechanisms. SO_4^{2-} does not increase iron solubility at 310 °C; instead, under the high-temperature reducing conditions of the system, SO_4^{2-} can be reduced to H_2S, which provides an additional cathodic pathway that promotes accelerated dissolution once sufficient sulphate is present.

- When Cl^- and SO_4^{2-} are both present at 310 °C, the combined accelerated corrosion threshold depends strongly on the initial chemical form of the contaminants. In the ammonium salt trials, the combined threshold was higher than for individual Cl^- contamination. In contrast, when the contaminants were introduced as mineral acids (HCl and H_2SO_4), the combined threshold was lower than that for HCl alone. Since ammonium salts are not expected to form beneath boiler tube deposits, mineral acids represent that more relevant form of contamination for future experimental studies.

- The accelerated corrosion thresholds reported here represent lower-bound values. Since the experiments were performed on initially unpassivated steel, the results reflect the most conservative case; passivated boiler tubing would be expected to exhibit higher thresholds, however, the mechanistic trends are expected to remain applicable.

- The mechanistic distinctions identified thermodynamic control for chloride, kinetic control for sulphate, and strong dependence on contaminant speciation, provide a foundation for improved boiler water chemistry guidelines. These results support ongoing efforts to develop mechanistically informed shutdown limits and predictive models for high-temperature corrosion under contaminant ingress.

5 ACKNOWLEDGEMENTS

The Electric Power Research Institute (EPRI), the International Association for the Properties of Water and Steam (IAPWS), and David Addison at Thermal Chemistry Ltd. are gratefully acknowledged for their financial support and collaboration with this work. The authors also acknowledge the contributions of the following individuals: Adon Briggs, for his extensive work in manufacturing the custom fittings and electrodes used throughout the study; Dr. Lihui Liu for her assistance with the ion chromatography analyses; and Brad McCann and Chester Morris, for their support in modifying and maintaining the test apparatus. Finally, the authors extend their gratitude to Siemens Heat Transfer Technology for providing a section of boiler tube from which the steel electrodes were machined.

6 REFERENCES

1. D. J. Flynn and Nalco Water, Eds., *The Nalco water handbook*, Fourth edition. New York: McGraw-Hill Education, 2018.
2. International Association for the Properties of Water and Steam, "Technical Guidance Document: Volatile treatments for the steam-water circuits of fossil and combined cycle/HRSG power plants." 2015.
3. P. 1912- Cohen, ASME Research and Technology Committee on Water and Steam in Thermal Power Systems., P. 1912- Cohen, and ASME Research and Technology Committee on Water and Steam in Thermal Power Systems., *The ASME handbook on water technology for thermal power systems*. New York, NY: American Society of Mechanical Engineers, 1989.
4. L.-B. Niu and K. Nakada, "Effect of chloride and sulfate ions in simulated boiler water on pitting corrosion behavior of 13Cr steel," *Corrosion Science*, vol. 96, pp. 171–177, Jul. 2015, doi: 10.1016/j.corsci.2015.04.005.
5. L.-B. Niu, K. Okano, S. Izumi, K. Shiokawa, M. Yamashita, and Y. Sakai, "Effect of chloride and sulfate ions on crevice corrosion behavior of low-pressure steam turbine materials," *Corrosion Science*, vol. 132, pp. 284–292, Mar. 2018, doi: 10.1016/j.corsci.2017.12.017.
6. D. Iravani and R. Arefinia, "Effectiveness of one-to-one phosphate to chloride molar ratio at different chloride and hydroxide concentrations for corrosion inhibition of carbon steel," *Construction and Building Materials*, vol. 233, p. 117200, Feb. 2020, doi: 10.1016/j.conbuildmat.2019.117200.
7. Z. Zhu, X. Jiao, X. Tang, and H. Lu, "Effects of SO42- concentration on corrosion behaviour of carbon steels," *Anti-Corrosion Methods and Materials*, vol. 62, no. 5, pp. 322–326, 2015, doi: 10.1108/ACMM-01-2014-1342.
8. L.-B. Niu, H. Kato, K. Shiokawa, K. Nakamura, M. Yamashita, and Y. Sakai, "Electrochemical Crevice Corrosion Behaviors of Low-Pressure Steam Turbine Materials in the Simulated Boiler Water Added Chloride and Sulfate Ions," *Materials Transactions*, vol. 54, no. 12, pp. 2225–2232, 2013, doi: 10.2320/matertrans.M2013202.
9. S. Xiong, Z. Zhu, and L. Jing, "Influence of Cl‐ ions on the pitting corrosion of boiler water‐wall tube and its principle," *Anti-Corrosion Methods and Materials*, vol. 59, no. 1, pp. 3‐9, Jan. 2012, doi: 10.1108/00035591211190481.
10. X. Wu, S. Huang, W. Zhang, Q. Feng, and Y. Huang, "Study on the electrochemical corrosion behavior of industrial boilers," *AIP Conference Proceedings*, vol. 1971, no. 1, p. 020024, Jun. 2018, doi: 10.1063/1.5041119.
11. B. O. Hasan and S. A. Sadek, "The effect of temperature and hydrodynamics on carbon steel corrosion and its inhibition in oxygenated acid–salt solution," *Journal of Industrial and Engineering Chemistry*, vol. 20, no. 1, pp. 297–307, Jan. 2014, doi: 10.1016/j.jiec.2013.03.034.
12. J. Macak, P. Sajdl, P. Kucera, and R. Novotny, In-situ study of high temperature aqueous corrosion by electrochemical techniques, *NACE Corrosion-2005*, Houston, Texas, 2005.
13. International Association for the Properties of Water and Steam, "Certified Research Need – ICRN#25: Corrosion mechanisms related to the presence of contaminants in steam/water circuits, particularly in boiler water." Jun. 2014.
14. B. A. James, L. D. Paul, and M. T. Miglin, "Low cycle fatigue crack initiation in SA-210 A1 carbon steel boiler tubing in contaminated boiler water," in *American Society of Mechanical Engineers, Pressure Vessels and Piping Division PVP*, 1990, pp. 13–19.
15. E. J. Simmons, "Use of the Pearson Bridge in Corrosion Inhibitor Evaluation," *Corrosion*, vol. 11, no. 6, pp. 25–30, Jun. 1955, doi: 10.5006/0010-9312-11.6.25.
16. R. V. Skold and T. E. Larson, "Measurement of the instantaneous corrosion rate by means of polarization data," *Corrosion*, vol. 13, no. 2, pp. 69–72, 1957.
17. M. Stern and A. L. Geary, "Electrochemical Polarization: I. A Theoretical Analysis of the Shape of Polarization Curves," *Journal of The Electrochemical Society*, p. 9, 1957, doi: 10.1149/1.2428496
18. M. Stern, "Electrochemical polarization: II. ferrous-ferric electrode kinetics on stainless steel," *Journal of The Electrochemical Society*, vol. 104, no. 9, p. 559, 1957, doi: 10.1149/1.2428653

19. M. Stern, “Electrochemical Polarization: III. Further Aspects of the Shape of Polarization Curves,” *Journal of The Electrochemical Society*, 1957, doi: 10.1149/1.2428438
20. M. Stern, “A Method for Determining Corrosion Rates from Linear Polarization Data,” *Corrosion*, vol. 14, no. 9, pp. 60–64, Sep. 1958, doi: 10.5006/0010-9312-14.9.60.
21. C. W. Bale et al., “FactSage thermochemical software and databases, 2010–2016,” *Calphad*, vol. 54, pp. 35–53, Sep. 2016, doi: 10.1016/j.calphad.2016.05.002.
22. E. McCafferty, *Introduction to corrosion science*, Springer Publishing 2010., doi: 10.1007/978-1-4419-0455-3.
23. F. Mansfeld, “The Effect of Uncompensated IR-Drop on Polarization Resistance Measurements,” *Corrosion*, vol. 32, no. 4, pp. 143–146, Apr. 1976, doi: 10.5006/0010-9312-32.4.143.
24. M. Berthold and S. Herrmann, “Investigations of Corrosion with Measurement and Compensation of the Ohmic Drop,” *Corrosion*, vol. 38, no. 5, pp. 241–245, May 1982, doi: 10.5006/1.3577345.
25. A. W. Colburn, K. J. Levey, D. O’Hare, and J. V. Macpherson, “Lifting the lid on the potentiostat: a beginner’s guide to understanding electrochemical circuitry and practical operation,” *Phys. Chem. Chem. Phys.*, vol. 23, no. 14, pp. 8100–8117, 2021, doi: 10.1039/D1CP00661D.
26. A. S. Quist and W. L. Marshall, “Assignment of Limiting Equivalent Conductances for Single Ions to 400°1,” *J. Phys. Chem.*, vol. 69, no. 9, pp. 2984–2987, Sep. 1965, doi: 10.1021/j100893a027.
27. A. J. Bard, L. R. Faulkner, and H. S. White, *Electrochemical methods: fundamentals and applications*, Third edition. Hoboken, NJ: John Wiley & Sons, Ltd., 2022.
28. International Association for the Properties of Water and Steam, “Technical Guidance Document: Phosphate and NaOH treatments for the steam-water circuits of drum boilers of fossil and combined cycle/HRSG power plants.” 2015.
29. D. H. Lister, and W. G. Cook, “Chapter 14: Nuclear Plant Materials and Corrosion,” in *The Essential CANDU, A Textbook on the CANDU Nuclear Power Plant Technology*, Editor-in-Chief Wm. J. Garland, University Network of Excellence in Nuclear Engineering (UNENE). ISBN 0-9730040. Retrieved from: https://www.unene.ca/education/candu-textbook on April 6, 2026.
30. T. Satoh, Y. Shao, W. G. Cook, D. H. Lister, and S. Uchida, “Flow-Assisted Corrosion of Carbon Steel Under Neutral Water Conditions,” *Corrosion*, vol. 63, no. 8, pp. 770–780, Aug. 2007, doi: 10.5006/1.3278426.
31. F. H. Sweeton and C. F. Baes, “The solubility of magnetite and hydrolysis of ferrous ion in aqueous solutions at elevated temperatures,” *The Journal of Chemical Thermodynamics*, vol. 2, no. 4, pp. 479–500, 1970.
32. P. R. Tremaine and J. C. LeBlanc, “The solubility of magnetite and the hydrolysis and oxidation of Fe2+ in water to 300°C,” *Journal of Solution Chemistry*, vol. 9, no. 6, pp. 415–442, Jun. 1980, doi: 10.1007/BF00645517.
33. S. E. Ziemniak, M. E. Jones, and K. E. S. Combs, “Magnetite solubility and phase stability in alkaline media at elevated temperatures,” *Journal of Solution Chemistry*, vol. 24, no. 9, pp. 837–877, 1995.
34. S. E. Traubenberg and R. T. Foley, “The Influence of Chloride and Sulfate Ions on the Corrosion of Iron in Sulfuric Acid,” *J. Electrochem. Soc.*, vol. 118, no. 7, p. 1066, 1971, doi: 10.1149/1.2408248.
35. R. M. Cornell, A. M. Posner, and J. P. Quirk, “Kinetics and Mechanisms of the Acid Dissolution of Goethite (a-FeOOH),” *Journal of Inorganic and Nuclear Chemistry*, vol. 38, no. 3, pp. 563–567, 1976, doi: 10.1016/0022-1902(76)80305-3.
36. R. J. Atkinson, A. M. Posner, and J. P. Quirk, “Adsorption of potential-determining ions at the ferric oxide-aqueous electrolyte interface,” *Journal of Physical Chemistry*, vol. 71, no. 3, pp. 550–558, Feb. 1967, doi: 10.1021/j100862a014.
37. P. S. Sidhu, “Dissolution of Iron Oxides and Oxyhydroxides in Hydrochloric and Perchloric Acids,” *Clays and Clay Minerals*, vol. 29, no. 4, pp. 269–276, 1981, doi: 10.1346/CCMN.1981.0290404.
38. B. Zhang et al., “Unmasking chloride attack on the passive film of metals,” *Nature Communications*, vol. 9, no. 1, p. 2559, Jul. 2018, doi: 10.1038/s41467-018-04942-x.
39. L. Truche et al., “Experimental reduction of aqueous sulphate by hydrogen under hydrothermal conditions: Implication for the nuclear waste storage,” *Geochimica et Cosmochimica Acta*, vol. 73, no. 16, pp. 4824–4835, Aug. 2009, doi: 10.1016/j.gca.2009.05.043.

40. E. L. Shock, D. C. Sassani, M. Willis, and D. A. Sverjensky, “Inorganic species in geologic fluids: Correlations among standard molal thermodynamic properties of aqueous ions and hydroxide complexes,” *Geochimica et Cosmochimica Acta*, vol. 61, no. 5, pp. 907–950, Mar. 1997, doi: 10.1016/S0016-7037(96)00339-0.
41. “*CRC Handbook of Chemistry and Physics: A Ready-Reference Book of Chemical and Physical Data*, 97th Edition,” ProtoView, vol. 3, no. 32, 2016.
42. R. G. Bates and G. D. Pinching, “Acidic dissociation constant of ammonium ion at 0 to 50 °C, and the base strength of ammonia,” *J. Res. Natl. Bur. Stan.*, vol. 42, no. 5, p. 419, May 1949, doi: 10.6028/jres.042.037.
43. R. G. Bates and G. D. Pinching, “Acidic dissociation constant and related thermodynamic quantities for monoethanolammonium ion in water from 0° to 50 °C,” *J. Res. Natl. Bur. Stan.*, vol. 46, no. 5, p. 349, May 1951, doi: 10.6028/jres.046.039.
44. G. Olofsson, “Thermodynamic quantities for the dissociation of the ammonium ion and for the ionization of aqueous ammonia over a wide temperature range,” *The Journal of Chemical Thermodynamics*, vol. 7, no. 6, pp. 507–514, Jun. 1975, doi: 10.1016/0021-9614(75)90183-4.
45. S. Ma’mun et al., “Experimental determination of monoethanolamine protonation constant and its temperature dependency,” *MATEC Web Conference.*, vol. 101, p. 02001, 2017, doi: 10.1051/matecconf/201710102001.
46. M. H. Moayed and R. C. Newman, “Deterioration in critical pitting temperature of 904L stainless steel by addition of sulfate ions,” *Corrosion Science*, vol. 48, no. 11, pp. 3513–3530, Nov. 2006, doi: 10.1016/j.corsci.2006.02.010.
47. I. L. Rosenfeld and I. S. Danilov, “Electrochemical aspects of pitting corrosion,” *Corrosion Science*, vol. 7, no. 3, pp. 129–142, Jan. 1967, doi: 10.1016/S0010-938X(67)80073-8.
48. H. P. Leckie and H. H. Uhlig, “Environmental Factors Affecting the Critical Potential for Pitting in 18–8 Stainless Steel,” *Journal of the Electrochemical Society.*, vol. 113, no. 12, p. 1262, 1966, doi: 10.1149/1.2423801.
49. N. Aouina et al., “Initiation and growth of a single pit on 316L stainless steel: Influence of SO_4^{2-} and ClO_4^- anions,” *Electrochimica Acta*, vol. 104, pp. 274–281, Aug. 2013, doi: 10.1016/j.electacta.2013.04.109.
50. T. Hong and M. Naumo, “The Effect of SO_4^{2-} Concentration in NaCl Solution on the Early Stages of Pitting Corrosion of Type 430 Stainless Steel,” *Corrosion Science*, vol. 39, no. 5, pp. 961–967, 1997, doi: 10.1016/S0010-938X(97)81161-4.
51. E. A. Abd El Meguid, N. A. Mahmoud, and S. S. Abd El Rehim, “The effect of some sulphur compounds on the pitting corrosion of type 304 stainless steel,” *Materials Chemistry and Physics*, vol. 63, no. 1, pp. 67–74, Feb. 2000, doi: 10.1016/S0254-0584(99)00206-0.